



# A modified dislocation density-based model of 30CrMnSiA considering the coupling effect of electroplasticity and grain refinement during the pulsed current-assisted plane strain deformation

Qinxiang Xia<sup>1,2</sup>, Can Chen<sup>1,2,\*</sup> , Gangfeng Xiao<sup>1,2,\*</sup>, Kaiwen Chen<sup>1,2</sup>, and Haoyang Zhou<sup>1,2</sup>

<sup>1</sup>School of Mechanical and Automotive Engineering, South China University of Technology, Guangzhou 510641, People's Republic of China

<sup>2</sup>Guangdong Provincial Key Laboratory of Precision Equipment and Manufacturing Technology, South China University of Technology, Guangzhou 510641, People's Republic of China

Received: 11 April 2023

Accepted: 15 July 2023

Published online:

2 August 2023

© The Author(s), under exclusive licence to Springer Science+Business Media, LLC, part of Springer Nature 2023

## ABSTRACT

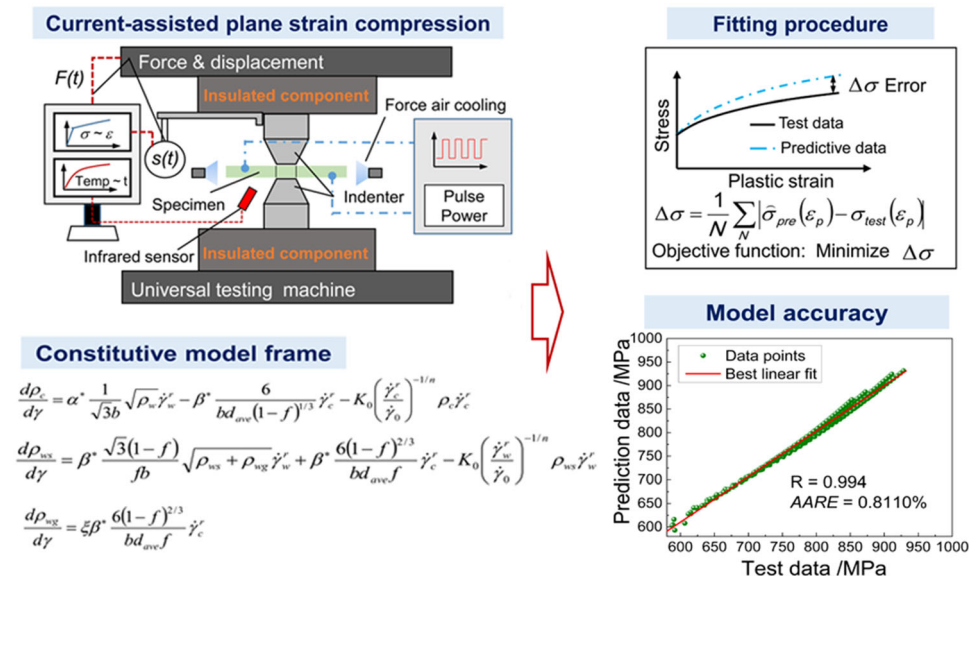
The large deformation of difficult-to-deform metal under pulsed currents involves the coupling effect of grain refinement and electroplasticity, making it challenging to capture the flow behavior accurately during severe plastic deformation. To develop a highly accurate constitutive model that accounts for the coupling effect, a current-assisted plane strain compression (CAPSC) test of 30CrMnSiA was carried out, using a peak current density ( $J_p$ ) range of 0–30 A mm<sup>-2</sup> and duty ratio ( $d$ ) of 0–20%. A microstructural observation was also performed via the EBSD test on the specimens after the CAPSC test. The result indicates that the true stress decreases significantly with increased  $J_p$  and  $d$ , descending to a stable value of 13% under high  $J_p$  and high  $d$  regions. Pulsed current accelerates grain refinement, promoting the transition from low-angle grain boundaries to high-angle grain boundaries through the recovery mechanism. Fine grain sizes increased from 31.7 to 45.5% in the pulsed-current condition compared to the non-current condition. Based on the above discovery, a physical-based constitutive model frame was proposed to characterize the independent evolution and transformation of dislocation density at the grain boundary and interior. Besides, the current density is also coupled into the model as an influence term of the material parameters to capture the influence of electroplasticity on grain refinement. Comparing the test stress to the predictive stress reveals that the model accurately predicts the CAPSC stress of 30CrMnSiA with a correlation coefficient of 0.974 and an average relative error of 4.56%.

Handling Editor: Megumi Kawasaki.

Address correspondence to E-mail: chencan\_nuaa@163.com; xiaogf@scut.edu.cn

<https://doi.org/10.1007/s10853-023-08792-x>

## GRAPHICAL ABSTRACT



## Introduction

Alloy structural steels are a class of difficult-to-deform metals at room temperature. They are extensively utilized in aerospace, transportation, and automated production because of their exceptional strength, hardness, and fatigue resistance [1]. However, alloy structural steel is not a lightweight and low-density metal. Consequently, these alloy structural steel components often need ultra-thin wall thicknesses for light weight and energy efficiency requirements. These ultra-thin structural components require better plasticity for forming process. Current-assisted forming (CAF) process is a novel type of forming method that makes use of the electroplastic effect to enhance plasticity [2], minimize deformation resistance [3], and reduce residual stress [4]. The mechanism of the electroplastic effect can typically be explained by local Joule heating effects and the changes in dislocation density storage, movement, and morphology induced by the pulsed current [5–7].

However, the CAF process for preparing ultra-thin structures involves a substantial amount of plastic deformation, leading to grain refinement of microstructure, such as the current-assisted flow spinning process (CAFS) [8]. Predicting the plastic deformation behavior during CAFS is still challenging because of the intricate coupling impact of grain refinement and the electroplastic effect. There is an inadequate theoretical basis for studying and modeling the deformation behavior during the CAFS process.

The constitutive model used to characterize deformation behavior serves as the theoretical foundation for analyzing and optimizing the forming process [9–11]. Several studies have demonstrated that a physical constitutive model based on the evolution of dislocation density can easily incorporate the effects of various microstructural change mechanisms and thereby describe the plastic deformation behavior of difficult-to-deform metals under the electroplastic effect [3, 12–15]. Zhao et al. investigated the deformation behavior of an ultra-thin nickel-

based superalloy using a current-assisted uniaxial tensile test [3]. The study introduced additional components related to the precipitation phase into the K-M dislocation evolution equation to correctly predict the plastic deformation behavior of high-temperature alloys under the coupling effect of high temperature and pulsed current. Liu et al. [13] studied the plastic deformation behavior of different grain-size nickel-based superalloy specimens. The dislocation model obtained by the study includes the grain size variable, which permits the influence of the initial microstructure on the electroplastic effect. However, there remains a limited understanding of the coupling mechanism between the grain refinement and the electroplastic effect. The necking phenomenon during tensile test results in a very short section of uniform plastic deformation [16]. During the tensile test, assessing the plastic deformation behavior with electroplasticity and significant grain refinement becomes impossible. The plane strain compression (PSC) test is an alternative mechanical test that can be employed to evaluate the flow stress of metals in the high strain range [17, 18]. Therefore, the PSC test is commonly utilized as a physical simulation test for the forming process involving large strain, such as multi-pass rolling and flow spinning. Another advantage of this test is that it creates a deformation state similar to the mentioned processes, i.e., the plate blank will compress in the normal direction (or thickness direction for spun cylindrical blank), elongate in the rolling direction (or axial direction) and the deformation in the transverse direction (or tangential direction) is almost negligible [19, 20]. This method also can investigate the microstructural changes during severe plastic deformation processes. Yin et al. and Annasam et al. [21, 22] studied the effect of microstructural evolution on macroscopic flow behavior at elevated temperatures based on plane strain compression experiments.

This study investigated the effect of coupling electroplasticity and grain refinement on hardening behavior using the current-assisted plane strain compression (CAPSC) tests and microstructure observation to reveal the mechanism of the effect of electroplasticity on grain refinement. Then, a dislocation density evolution model was developed that accounted for the electroplastic effect and grain refinement during large strains. The findings provide insight into the interaction between electroplasticity, strain-induced grain refinement, and strain-

strengthening mechanisms during plastic deformation. This study promotes the industrialized application of current-assisted severe plastic deformation processes for manufacturing thin-walled parts, such as current-assisted multi-rolling and CAFS.

## Experimental details

### Specimen preparation

The experimental material chosen for the study was annealed 30CrMnSiA with a 2 mm thickness. The chemical composition of the material is presented in Table 1. The specimen for the CAPSC test was obtained using an EDM wire-cutting machine. Figure 1a provides the geometric size of the initial specimen, which had a dog-bone shape to permit the introduction of a pulsed current at both sides. The initial microstructure of the cross-section of 30CrMnSiA was analyzed through optical microscopy after etching using a solution of 3% HNO<sub>3</sub>, 1% C<sub>2</sub>H<sub>6</sub>O, and 96% H<sub>2</sub>O. It was observed that the microstructures were composed of laminar pearlite and  $\alpha$ -ferrite, as shown in Fig. 1b. The average grain size of the initial microstructure was determined using the linear intercept method described as described in ASTM E112-10 standard [23], and the average grain size was estimated to be approximately 16  $\mu$ m.

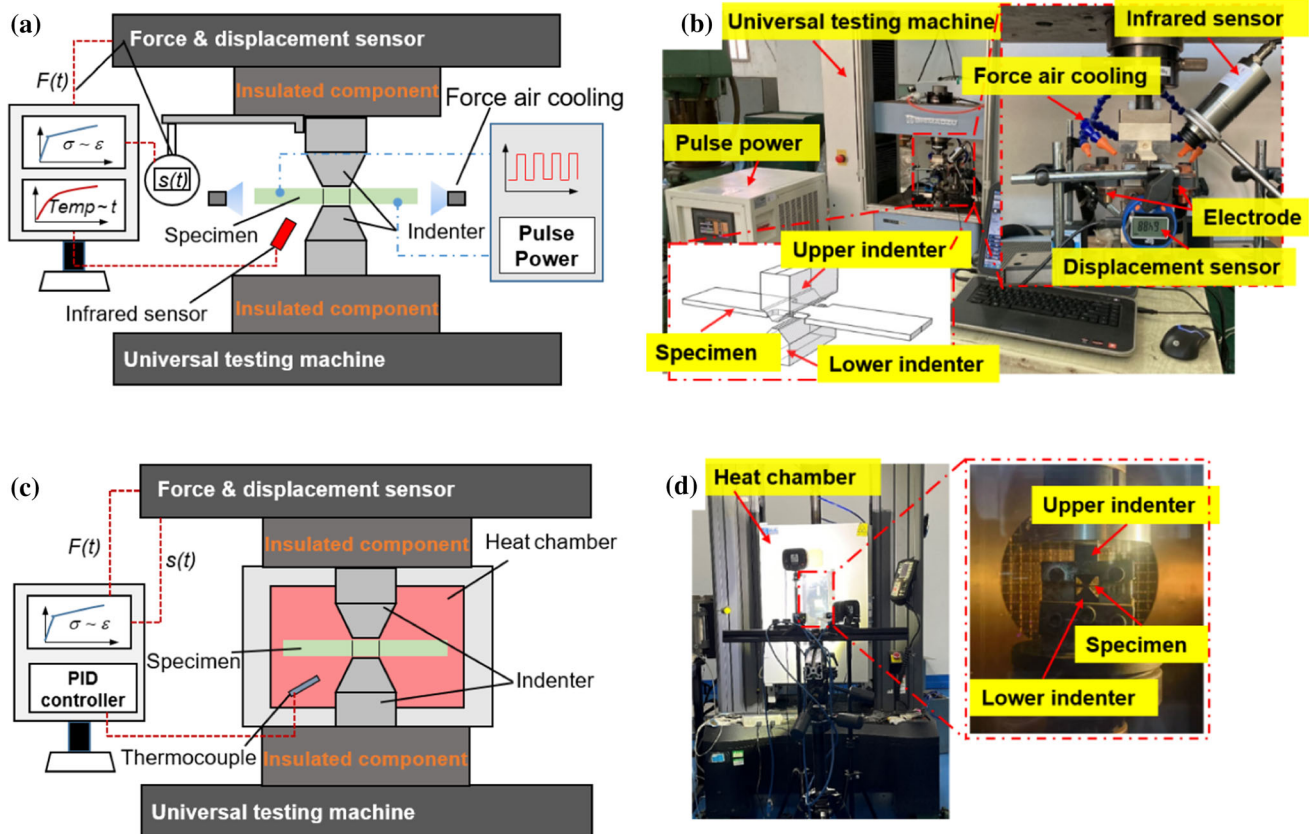
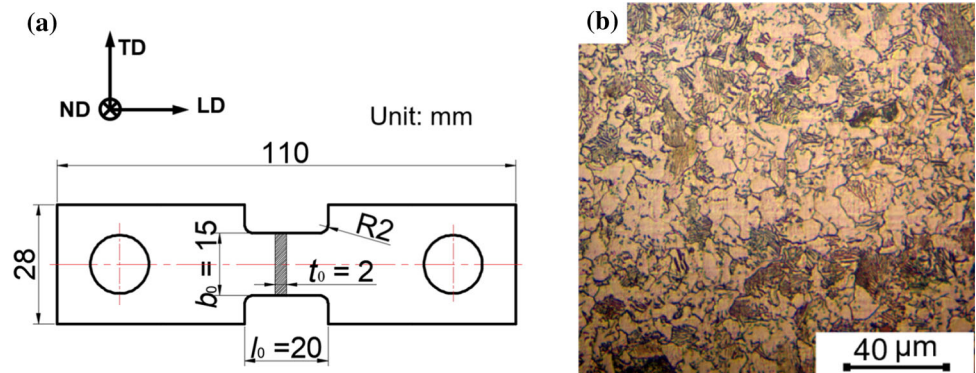
### CAPSC test setup and parameters

Figure 2a–b shows the schematic and CAPSC setup used in this study, which was conducted on a Shimadzu AG-plus 100kN UTM. The geometric size of the indenter can be found in previous work [24]. A pulsed current was applied between the two ends of the specimen using a pulsed power supply (NHWYM-5-1000,  $f = 100$  Hz). The specimen thickness was 2 mm, making the temperature difference negligible along the thickness direction. To record the surface temperature variation, an infrared sensor was used, and the surface of the specimen was cooled

**Table 1** Chemical composition of 30CrMnSiA (in wt%)

C	Si	Mn	Cr	S	P	Ni	Cu	Mo
0.30	1.08	0.91	0.95	0.01	0.01	0.02	0.01	0.03

**Figure 1** Specimen preparation and microstructure characterization: **a** Geometric size and **b** initial microstructure of the 30CrMnSiA.



**Figure 2** CAPSC test system: **a** schematic of CAPSC; **b** actual setup of CAPSC and TAPSC test; **c** schematic of TAPSC; **d** actual setup of TAPSC.

with compressed air. The infrared sensor measured 0–550 °C with an error range of  $\pm 3$  °C.

As a physical simulation of quasi-static deformation processes such as flow spinning or rolling, the strain rate range for the PSC tests is generally chosen to be in the range of 0.001–0.1  $s^{-1}$  [19, 20]. Considering that alloy steel is a rate-insensitive material under insignificant Joule heat conditions, a median value of 0.01  $s^{-1}$  was chosen as the strain rate for the

test. For steel materials, the thermal effect from the pulsed current will gradually increase significantly after the peak current density  $J_p > 5$   $A\ mm^{-2}$  and duty ratio  $d > 20\%$  [18, 24, 25]. In order to avoid the influence of excessive Joule heating on test results, the peak current density ( $J_p$ ) was set to 0, 1.25, 2.5, 3.75 and 5  $A\ mm^{-2}$  with a fixed duty ratio  $d$  of 20%; the duty ratio ( $d$ ) was set to 0, 5, 10, 15 and 20% with a fixed peak current density  $J_p$  of 5  $A\ mm^{-2}$ . Non-



current (NC) compression corresponds to the test condition of  $J_p = 0 \text{ A mm}^{-2}$ ,  $d = 0\%$ . Then,  $J_p$  is gradually increased at intervals of  $10 \text{ A mm}^{-2}$  up to  $30 \text{ A mm}^{-2}$  as an extra test set to determine the limit of electroplasticity. Figure 2c–d shows that a thermally-assisted plane strain compression (TAPSC) test was also conducted to evaluate the Joule heating effect on plastic behavior induced by the pulsed current. The TAPSC test temperature was steady at  $135 \text{ }^\circ\text{C} \pm 3 \text{ }^\circ\text{C}$ , the highest temperature measured in CAPSC tests.

The electron backscattered diffraction tests (EBSD, acceleration voltage of 20 kV, step sizes of  $0.12 \text{ }\mu\text{m}$ ) were carried out on the LD-ND plane of the deformed specimens under no-current and pulsed current-assisted conditions ( $J_p = 30 \text{ A mm}^{-2}$ ,  $d = 20\%$ ) after compression, as shown in Fig. 3. The EBSD data was processed using Channel 5 software and the MATLAB-based open-source package tool MTEX [26]. A critical misorientation angle  $\theta$  of  $15^\circ$  was used to define the grains and determine the different boundary types. Accordingly, the low-angle grain boundaries (LAGBs) were defined as  $\theta = 5\text{--}15^\circ$  boundaries, while the high-angle grain boundaries (HAGBs) were defined as  $\theta > 15^\circ$  boundaries [27].

## Test results

### Plastic hardening behavior during CAPSC test

Figure 4 shows the true stress ( $\sigma$ )–plastic strain ( $\epsilon_p$ ) curves under different current conditions during

CAPSC, which were calculated from the force and displacement data of the test system using a formula described in the literature [17]. Figure 5 shows the specimen temperature variation under different current conditions during the test. Each temperature curve has two distinct stages: rising and stable. The testing machine load was applied 120 s after the pulsed power was provided to ensure that the specimen temperature reached equilibrium. The maximum reduction in true stress is around 13% under a pulsed current condition of  $J_p = 30 \text{ A mm}^{-2}$ ,  $d = 20\%$  when true plastic strain  $\epsilon_p = 1.2$ . Meanwhile, the temperature gradually increases as  $J_p$  and  $d$  increase. It is commonly acknowledged that the stress reduction generated by the pulsed current can be attributed to the thermal softening caused by Joule heating and the electroplastic effect [3, 28]. The proportional contribution of the two factors above to stress reduction varies between materials and test settings [14]. As can be seen in Fig. 5, the maximum temperature during the CAPSC test was around  $135 \text{ }^\circ\text{C}$  (corresponding to the parameters of  $J_p = 30 \text{ A mm}^{-2}$ ,  $d = 20\%$ ). In comparison, the maximum reduction of the true stress is only 2.04% in the TAPSC test, indicated by the red line in Fig. 4a. For conventional structural steel, thermally-induced stress reduction ranged from 100 to  $200 \text{ }^\circ\text{C}$  has been reported to be about 2–4% by Waibhaw et al. [29]. Therefore, the pulsed current effect dominates the stress reduction of 30CrMnSiA during the CAPSC test within the set current parameters, whereas the Joule heating effect contributes less to the reduction.

Similar to the test results of Zhao et al. [3], the true stress does not considerably decrease as the  $d$  rises

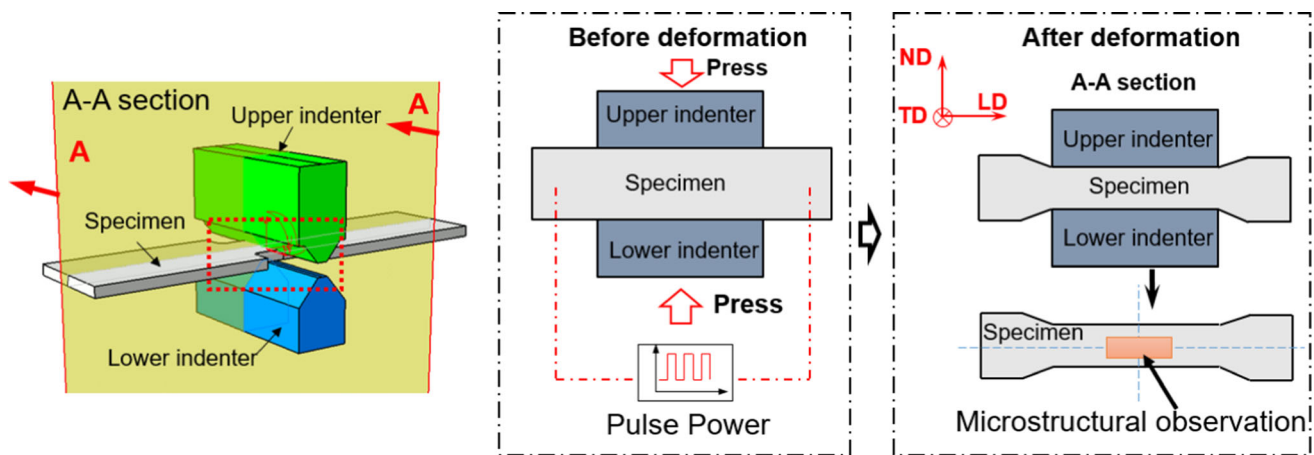


**Figure 3** Sampling location of EBSD sample at deformed specimen.

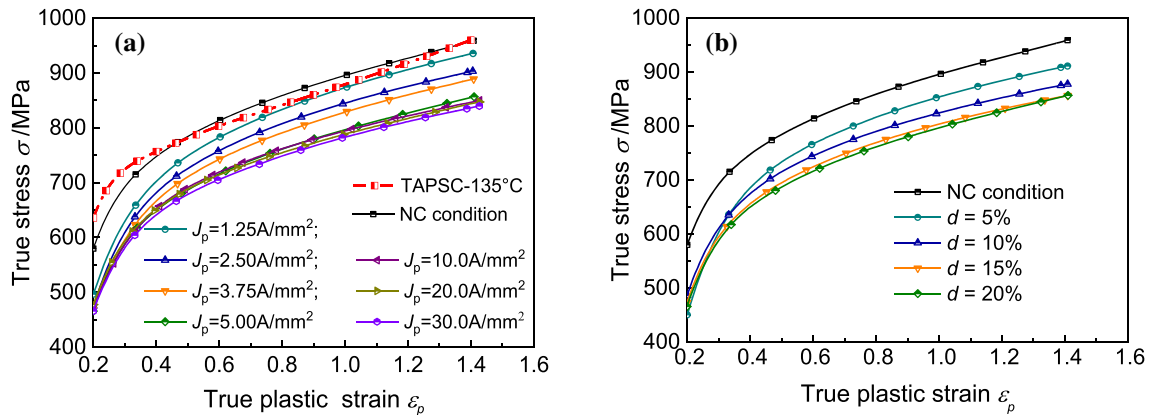


**Figure 4** True stress—plastic strain curves under **a** different  $J_p$  of 0–30  $\text{A mm}^{-2}$  when the  $d$  is equal to 20% and **b** different  $d$  of 0–20% when  $J_p$  is equal to 5  $\text{A mm}^{-2}$ .

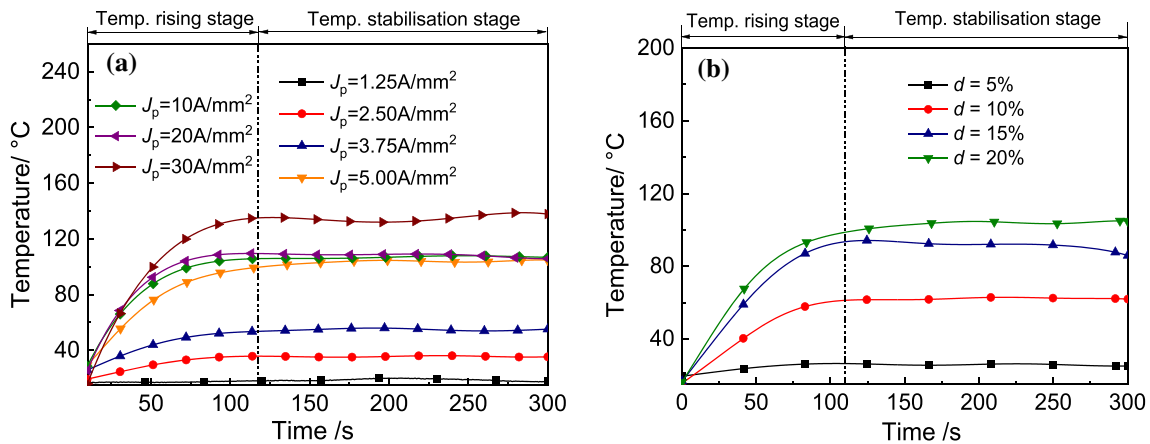


**Figure 5** Measured surface temperatures of specimen under different current parameters: **a** different peak current densities and **b** different duty ratios.

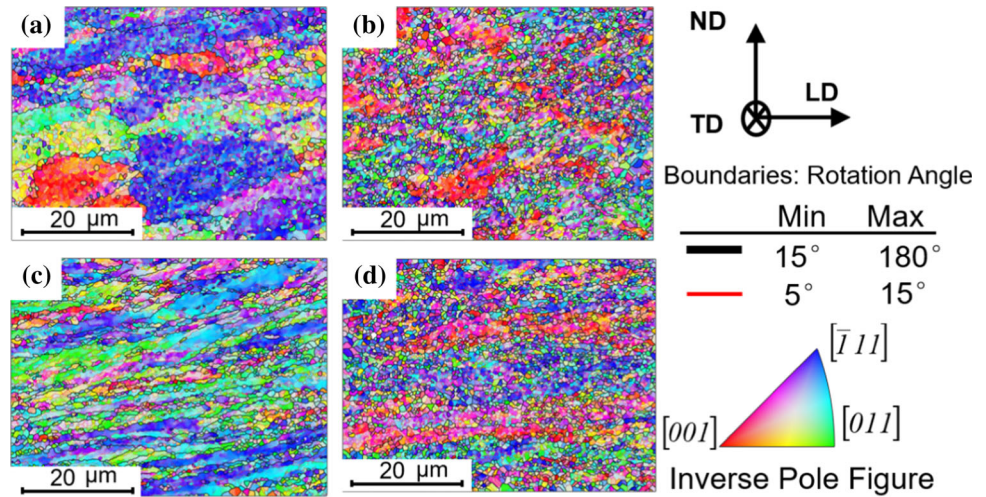
from 15 to 20% with almost the same value. It indicates that  $J_p$  and  $d$  have insignificant effect on stress reduction once they have achieved a crucial saturation [30]. The premise of the conclusion is that the temperature rise effect of the test is insignificant. According to Molotskii et al. [31], the pinned dislocations are unpinned by the current-induced magnetic field, reducing dislocation motion resistance. To describe the short-range stress subject to the electroplastic effect, Xu et al. [14] proposed a uniformed equation based on Molotskii theory that includes a logarithmic functional term for the current density to describe the short-range stress subject to the electroplastic effect. The equation illustrates that as current density increases, the number of pinning bonds that can be unpinned by the current steadily decreases. More electrical energy will be converted into heat dissipation. Therefore, when the current density

increases to the point where significant temperature rise effects occur, the Joule heating effect caused by the current will gradually become the main factor in the decrease of stress, as reported in most research [5, 32, 33].

### Microstructure observation of CAPSC test

Figure 6 shows the EBSD grain orientation diagram at  $\epsilon_p = 0.8$  and 1.2 under the non-current (NC) and pulsed current of  $J_p = 30 \text{ A mm}^{-2}$ ,  $d = 20\%$  (PC) conditions. The HAGB and LAGB are denoted by black and red lines, respectively. The microstructure of the specimens evolved from coarse grains to refined grains compressed along the ND direction after deformation. The mechanism of microstructural evolution during the severe forming process is primarily regarded as strain-induced grain refinement.

**Figure 6** Orientation maps of 30CrMnSiA under different test conditions: **a** NC at  $\epsilon_p = 0.8$ , **b** NC at  $\epsilon_p = 1.2$ , **c** PC at  $\epsilon_p = 0.8$  and **d** PC at  $\epsilon_p = 1.2$ .



The schematic of the mechanism is presented in Fig. 7. The original coarse grains (Stage I) gradually produce dislocation cells and LAGBs (Stage II) through dislocation entanglement and accumulation mechanisms in the early deformation stage; with further plastic deformation, the dislocation cells or LAGBs gradually transform into HAGBs, thus achieving grain refinement (Stage III) [34]. At the same plastic strain deformation, the degree of coarse grain deformation under the PC condition is more significant than that in the NC condition, as shown in Fig. 6c versus a, as well as Fig. 6d versus b. It is reasonable to assume that the pulsed current effect reduces slip resistance and induces grain conversion from the hard phase to the soft phase, which is beneficial to even deformation [32].

The pulsed current also significantly impacts the grain size distribution in the microstructure. Figure 8 shows the grain size distribution of deformed specimens under different conditions. The lognormal function can fit the grain size distributions, as shown

in Fig. 8, with the red curves. The black curves in Fig. 8 represent the cumulative frequency obtained by integrating the frequency distribution function. The above EBSD data calculated the three parameters,  $D_{mean}$ ,  $D_{50}$ , and  $D_{90}$ , to evaluate the grain size distribution [35].  $D_{mean}$  is the mathematical expectation of the distribution function and represents the weighted average of all grain sizes.  $D_{50}$  represents the diameter corresponding to a cumulative frequency of 50%, i.e., the median in statistics. Similarly,  $D_{90}$  was also evaluated.  $D_{50}$  and  $D_{90}$  are clearly close for both conditions at  $\epsilon_p = 1.2$ , at about 0.64  $\mu\text{m}$  and 1.27  $\mu\text{m}$ , respectively. It indicates no statistically significant difference in overall average grain size.

However, the  $D_{mean}$  under the PC condition was significantly lower than that under the NC condition at the same deformation condition, decreasing from 1.87 to 1.56  $\mu\text{m}$  at  $\epsilon_p = 0.8$  or from 0.68 to 0.58  $\mu\text{m}$  at  $\epsilon_p = 1.2$ . The result shows more fine grains under the PC condition than under the NC condition. The percentage of fine grain sizes (smaller than

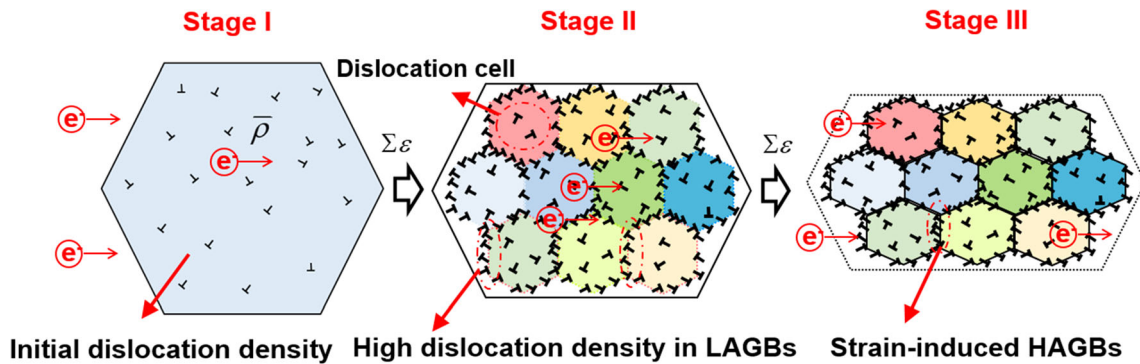


**Figure 7** Schematic model of strain-induced grain refinement mechanism under severe plastic deformation condition.

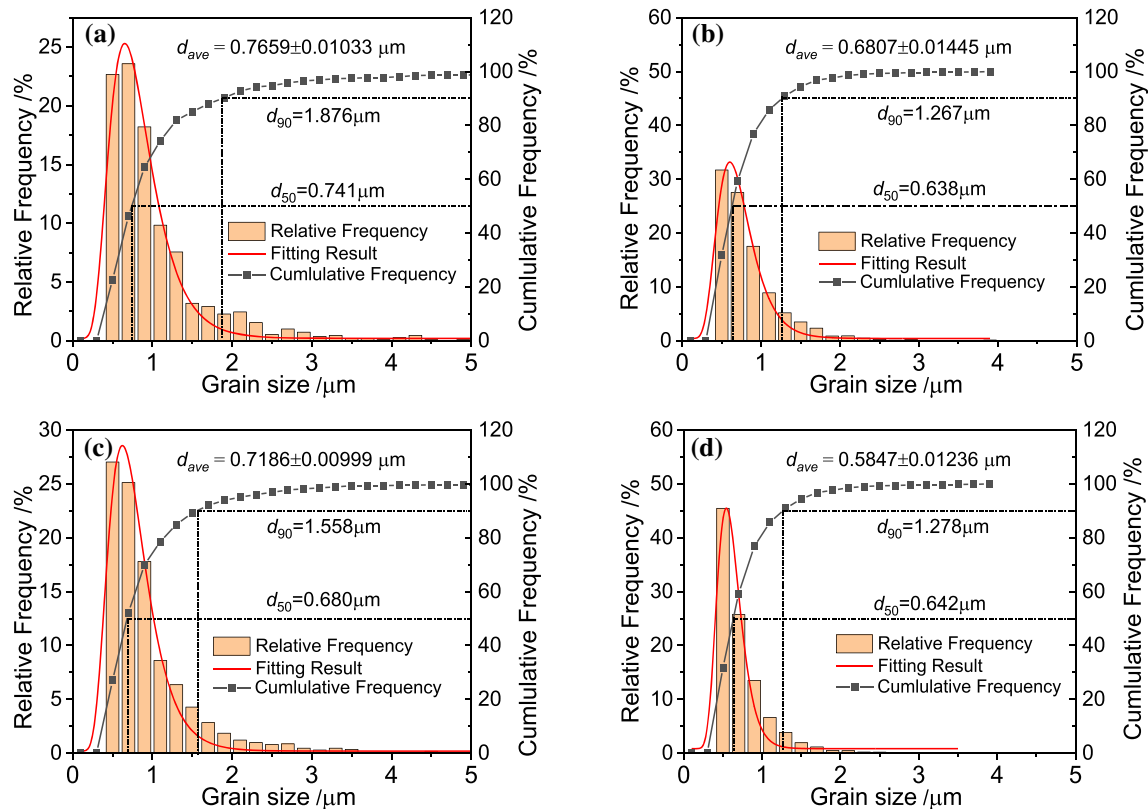


**Figure 8** Grain size distribution of 30CrMnSiA alloy structural steel under different test conditions: **a** NC at  $\epsilon_p = 0.8$ , **b** NC at  $\epsilon_p = 1.2$ , **c** PC at  $\epsilon_p = 0.8$  and **d** PC at  $\epsilon_p = 1.2$ .

0.5  $\mu\text{m}$ ) increased from 27.3% under the NC condition to 45.5% under the PC condition, respectively. Because local high current density regions exist near the grain boundary region of refinement grains, this may result in low-temperature dynamic recrystallization [5, 6, 15]. High pulsed current density produces extra non-thermal driving forces that promote diffusion. The additional driving force  $F_e^-$  generated by the pulsed current raises the activation energy of the atoms. It also encourages atomic to climb the barriers [12, 36], resulting in dynamic recovery. As a result, dislocations climb and arrange themselves as HAGBs, facilitating stage III of the grain refinement process depicted in Fig. 7 and resulting in a higher percentage of fine-grain [5].

### Effect of pulsed current on microstructure evolution mechanism during CAPSC test

To evaluate the effect of pulsed current on the grain refinement mechanism during CAPSC, the kernel average misorientation (KAM) and geometrically necessary dislocations (GND) were calculated based

on the EBSD data. The KAM was used to determine the average misorientation between the center and adjacent pixels, ranging from  $0^\circ$  to  $5^\circ$ . This method is commonly used to estimate local misorientation. The KAM value was used to calculate the GND required for the plastic deformation process. The formula for determining the GND density is given below [37]:

$$\rho_{\text{GND}} = 2\text{KAM}/\mu b \quad (1)$$

where,  $\rho_{\text{GND}}$  is the geometrically necessary dislocations.  $\mu$  represents the step of the EBSD data and  $b$  is the burgers vector.  $b$  is equal to  $2.58 \times 10^{-10}$  m for BCC material [38]. Figure 9 shows the GND maps under different conditions. Many LAGBs (red lines) are included inside the grain of Fig. 9a, indicating that the region is in initial stage II of grain refinement at  $\epsilon_p = 0.8$ , the formation stage of sub-grain boundaries and dislocation cells, as shown in Fig. 7. Figure 9b indicates that stages II and III of grain refinement can be observed, as there is still a large amount of GND density inside the grains, proving that the grain refinement is not fully completed under the NC condition. However, grain refinement stages



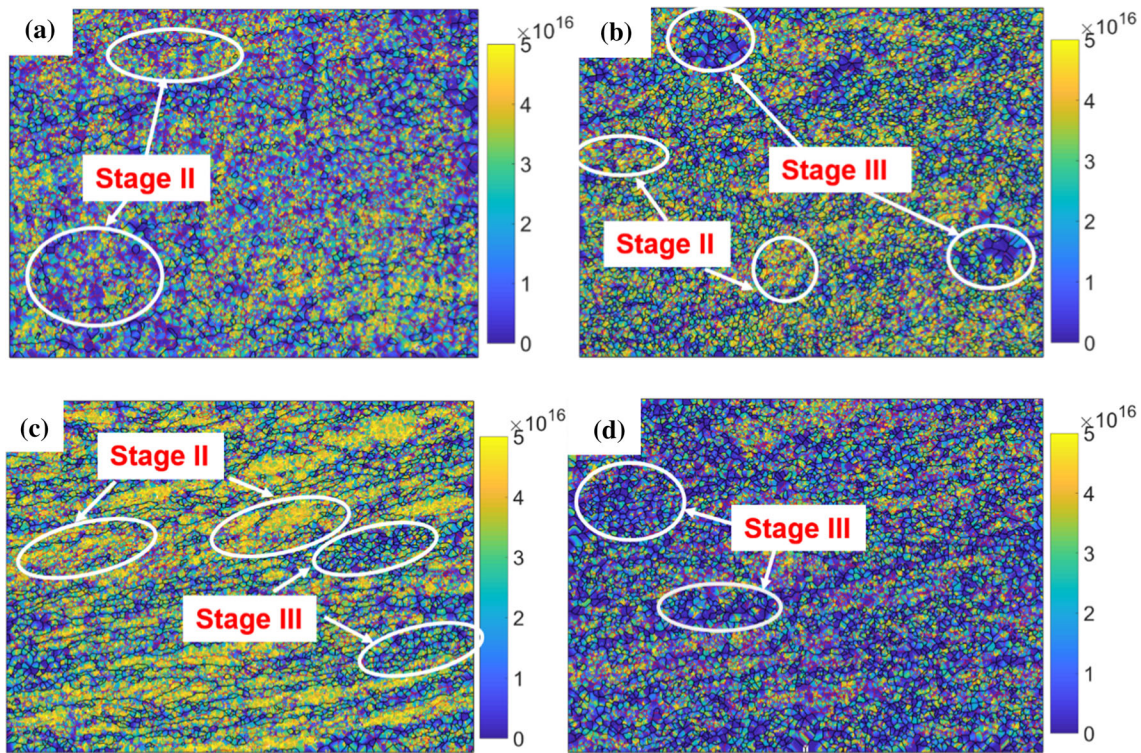


**Figure 9** GND map of 30CrMnSiA alloy structural steel under different test conditions: **a** NC at  $\varepsilon_p = 0.8$ , **b** NC at  $\varepsilon_p = 1.2$ , **c** PC at  $\varepsilon_p = 0.8$  and **d** PC at  $\varepsilon_p = 1.2$ .

II and III already exist simultaneously at  $\varepsilon_p = 0.8$  under the PC condition (Fig. 9c), and grain refinement is fully completed at  $\varepsilon_p = 1.2$  (Fig. 9d). Compared to Fig. 9b, there is less GND density inside the grains in Fig. 9d. It shows a decrease in mean GND from  $2.24 \times 10^{16} \text{ m}^{-2}$  in Fig. 9b to  $1.58 \times 10^{16} \text{ m}^{-2}$  in Fig. 9d.

Figure 10 shows the frequency distribution of misorientation angles under different conditions. The percentage of LAGBs and HAGBs under NC and PC conditions varies correspondingly with increasing strain. Specifically, LAGBs decrease with increasing strain, whereas HAGBs increase with increasing strain. The pulsed current has an evident effect on grain refinement. The percentage of LAGBs of NC conditions decreases from 40.6 to 28.6% of PC conditions at  $\varepsilon_p = 0.8$ , while there is an increase in HAGBs from 27.1 to 41.7%. At the final stage of deformation ( $\varepsilon_p = 1.2$ ), both percentages of HAGBs and LAGBs under the PC condition are higher than that under the NC condition, which is different from the situation at  $\varepsilon_p = 0.8$ . It indicates that the pulsed current effect on the grain refinement mechanism differs at various strains. The pulsed current boosts the rotation speed ( $\omega$ ) of grains and sub-grains,

decreasing grain boundary energy. As a result, grain misorientation increases, promoting the transformation of both LAGBs and HAGBs in a manner akin to the recovery effect of microstructure [39], as shown in Fig. 11. However, refining the grains further becomes difficult at the final stage of deformation when the percentage of HAGBs is close to saturation [40]. In this case, the pulsed current effect mainly accelerates the transition from local misorientation to LAGBs, leading to a higher proportion of LAGBs under the PC condition at high strain.

### Modified dislocation density-based constitutive model

#### Dislocation density-based constitutive model of microstructure evolution under no-current condition

It is clear that the CAPSC test is subject to the electroplastic effect, and the grain refinement is obvious. During this process, dislocation cells within the grains continuously accumulate and transform into HAGBs with increasing plastic strain. The high-

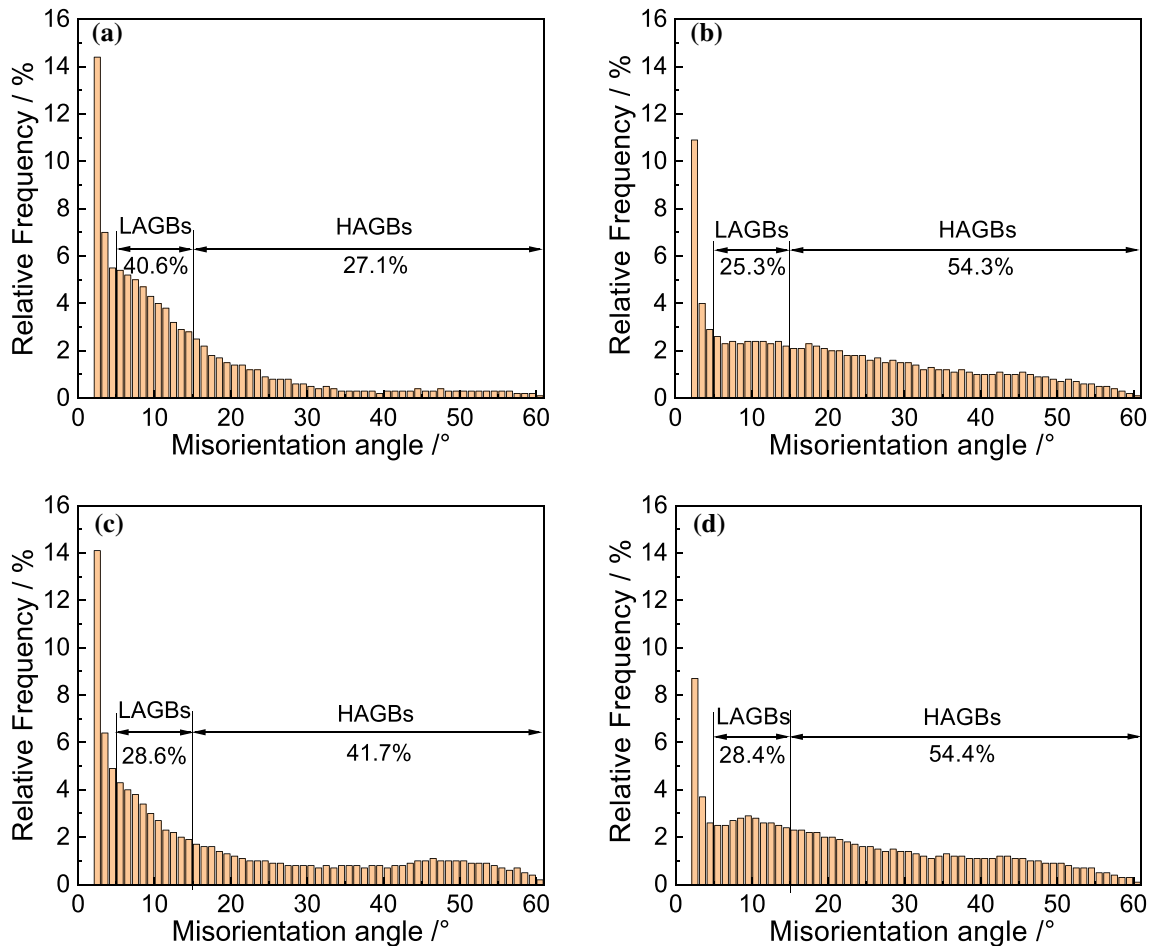


**Figure 10** Misorientation angle distributions under different test conditions: **a** NC at  $\epsilon_p = 0.8$ , **b** NC at  $\epsilon_p = 1.2$ , **c** PC at  $\epsilon_p = 0.8$  and **d** PC at  $\epsilon_p = 1.2$ .

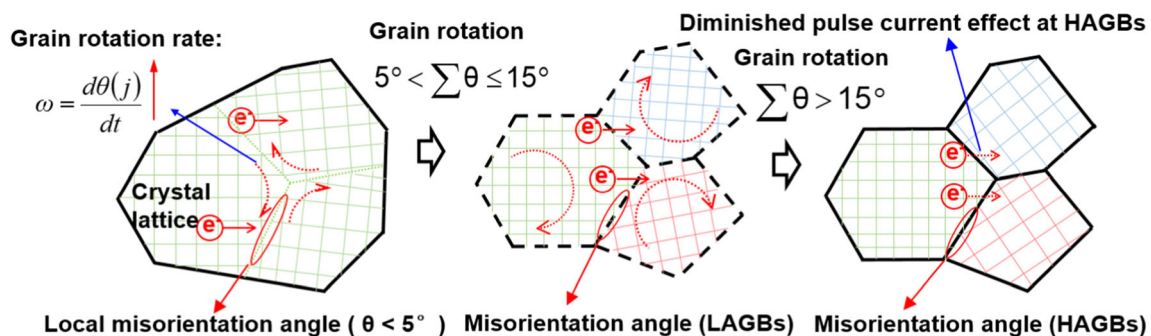


**Figure 11** Schematic diagram of the pulsed current effect on the transformation of LAGBs and HAGBs during CAPSC test.

energy pulsed current also significantly accelerates this process. To accurately characterize the transformation mechanism of dislocation density in grains and boundaries during severe plastic deformation, Estrin and Toth et al. [41] proposed a dislocation density evolution model based on the K-M dislocation density model. The physical-based model

accurately predicted the hardening behavior and microstructure evolution of grain size in a variety of forming processes, including multi-pass rolling at room temperature with significant plastic deformation and grain refinement [40, 42]. The dynamic evolution equations of dislocation density between grain interior and grain boundary are modified into

three coupled differential equations. The model reveals a complex mechanism of dislocation accumulation, annihilation, and microstructure evolution during deformation [40]:

$$\frac{d\rho_c}{d\gamma} = \alpha^* \frac{1}{\sqrt{3}b} \sqrt{\rho_w} \dot{\gamma}_w^r - \beta^* \frac{6}{bd_{ave}(1-f)^{1/3}} \dot{\gamma}_c^r - K_0 \left(\frac{\dot{\gamma}_c^r}{\dot{\gamma}_0}\right)^{-1/n} \rho_c \dot{\gamma}_c^r \tag{2}$$

$$\frac{d\rho_{ws}}{d\gamma} = \beta^* \frac{\sqrt{3}(1-f)}{fb} \sqrt{\rho_{ws} + \rho_{wg}} \dot{\gamma}_w^r + \beta^* \frac{6(1-f)^{2/3}}{bd_{ave}f} \dot{\gamma}_c^r - K_0 \left(\frac{\dot{\gamma}_w^r}{\dot{\gamma}_0}\right)^{-1/n} \rho_{ws} \dot{\gamma}_w^r \tag{3}$$

$$\frac{d\rho_{wg}}{d\gamma} = \xi \beta^* \frac{6(1-f)^{2/3}}{bd_{ave}f} \dot{\gamma}_c^r \tag{4}$$

where,  $\rho_{ws}$  and  $\rho_{wg}$  represent the statistical dislocation density and geometrically necessary density of grain boundaries, respectively. The sum of them is the grain boundary dislocation density:  $\rho_w = \rho_{ws} + \rho_{wg}$ .  $\gamma$  represents the shear strain. The model uses shear strain as the independent variable of the three equations because shear stress and shear deformation cause Frank-Read dislocation multiplication and slip. The first term in Eqs. (2) and (3) represents the Frank-Read source-activated dislocations. The second term indicates the number of interior grain dislocations that are transformed into grain boundary dislocations, and the third term represents the rate of dislocation annihilation due to recovery. As shown in Eq. (4), a portion (scale factor  $\xi = 0.01$ ) of the grain boundary dislocation is transformed to the geometrically necessary density, and the rest is the statistical dislocation density [40].  $\alpha^*$ ,  $\beta^*$  and  $K_0$  are the fitting parameters of the model.  $b$  is the burgers vector, and  $f$  denotes the volume fraction of grain boundaries in the microstructure. The resolved shear strain rates in the grain boundary and grain interior are denoted by  $\dot{\gamma}_w$  and  $\dot{\gamma}_c$ , respectively. To meet the requirement of strain compatibility, the resolved shear strain rate of grain interior and boundary should be consistent, i.e.  $\dot{\gamma}_w^r = \dot{\gamma}_c^r = \dot{\gamma}^r$ .  $\dot{\gamma}_0$  is a material constant called the reference resolved shear strain rate.  $d_{ave}$  represents the average grain size of the microstructure predicted by the model, which can be calculated as follow:

$$d_{ave} = K/\sqrt{\rho_{tot}} \tag{5}$$

where,  $K$  is a material constant and is equal to 10 for the ferrite phase [40].  $\rho_{tot}$  is the total dislocation density. Based on the rule of mixtures, the total dislocation density can be estimated as follows:

$$\rho_{tot} = f\rho_w + (1-f)\rho_c \tag{6}$$

The volume fraction  $f$  of the grain boundary gradually decreases with the increasing strain and approaches a stable value after reaching the high-strain region, which can be expressed as an exponential function as follows [41, 43]:

$$f = f_\infty + (f_0 - f_\infty) \cdot \exp\left(\frac{-\gamma}{\tilde{\gamma}}\right) \tag{7}$$

where,  $f_0$  and  $f_\infty$  represents the initial grain boundary volume fraction and the grain boundary volume fraction in the steady state stage, respectively. According to reference, the  $f_0$  and  $f_\infty$  value for steel are 0.29 and 0.077, respectively [40].  $\tilde{\gamma}$  is a model parameter that affects the rate at which the  $f$  decreases with increasing strain.

Besides, the resolved shear stress in grain interior  $\tau_c^r$  and grain boundary  $\tau_w^r$  are related to dislocation density and resolved strain rate as described below:

$$\tau_w^r = \alpha Gb\sqrt{\rho_w} \left(\frac{\dot{\gamma}_w^r}{\dot{\gamma}_0}\right)^{\frac{1}{m}} \tag{8}$$

$$\tau_c^r = \alpha Gb\sqrt{\rho_c} \left(\frac{\dot{\gamma}_c^r}{\dot{\gamma}_0}\right)^{\frac{1}{m}} \tag{9}$$

where,  $m$  represents the rate sensitivity index and it is a material parameter.  $G$  is the shear modulus. Also, the total resolved shear stress satisfies the volume rule of the mixture:

$$\tau^r = f\tau_w^r + (1-f)\tau_c^r \tag{10}$$

At last, the model believes that the stress caused by dislocation interaction can be decomposed into internal stress  $\sigma_i$  due to long-range obstacles and yield stress  $\sigma_0$  due to short-range obstacles [44]:

$$\sigma = \sigma_0 + \sigma_i \tag{11}$$

According to the principle of equivalent plastic deformation work, the relationship between the internal stress and the resolved shear stress can be obtained:  $\sigma_i = M\tau^r$ . Similarly,  $\dot{\gamma}^r = M\dot{\epsilon}$ , where  $\dot{\epsilon}$  represents the equivalent plastic strain rate. However, the model is rate-independent and is taken as 0.01 s<sup>-1</sup> in this study since the temperature rise is insignificant.  $\sigma_0$  is the yield stress contribution associated



with obstacles, such as precipitates, commonly a material constant.

The parameter fitting of the constitutive model adopts a comprehensive algorithm combining the Levenberg–Marquardt optimization algorithm and the Runge–Kutta numerical solution method for a differential equation set based on MATLAB software, as shown in Fig. 12. Equation (7) associated with the solution variable  $\gamma$  is rewritten as a differential equation for the convenience of the solution, i.e.:

$$\frac{df}{d\gamma} = (f_0 - f_\infty) \cdot \exp\left(\frac{-\gamma}{\tilde{\gamma}}\right) \cdot \left(\frac{-1}{\tilde{\gamma}}\right) \quad (12)$$

Equations (2)–(4) and (12) are a set of differential equations related to resolved shear strain  $\gamma$ . It can be solved using the Runge–Kutta numerical method if

the model parameters are determined. The objective function of the model fitting method is to optimize the material parameters to minimize the error between the test stress  $\sigma_{test}$  and the predicted stress  $\sigma_{pre}$ . The algorithm is fitted as follows. The material constants of the model are determined from the literature, as shown in Table 2. The table mainly shows the material constants of the ferrite phase of 30CrMnSiA. An iterative algorithm is adopted to fit the material parameters shown in Table 3. The optimization objective of the algorithm is to minimize the overall stress deviation value, and the optimization function is:

$$\min \Delta\sigma = \frac{1}{N} \left( \sum_{i=1}^N |\sigma_{pre} - \sigma_{test}| \right) \quad (13)$$

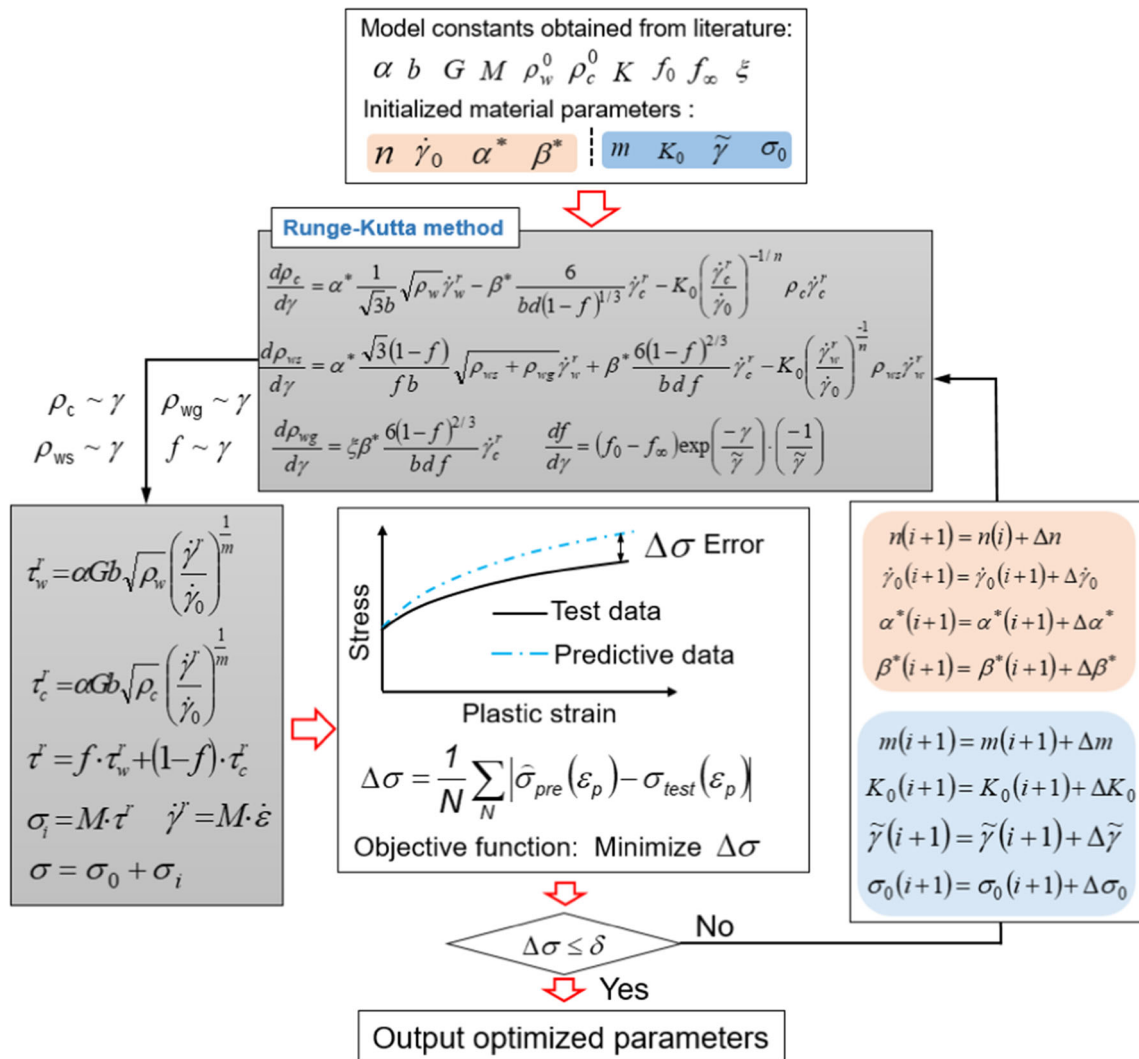


Figure 12 Fitting procedures of dislocation density evolution model.



**Table 2** Material constants of the constitutive model [3, 40]

$\alpha$	$b$	$G$	$M$	$K$	$f_0$	$f_\infty$	$\zeta$	$\rho_w^0/\text{m}^{-2}$	$\rho_c^0/\text{m}^{-2}$
0.25	2.58E-10	85,246	3.06	10	0.29	0.077	0.01	1.194E12	1.194E12

**Table 3** Material parameters of constitutive model under non-current condition

$n$	$\dot{\gamma}_0/\text{s}^{-1}$	$\alpha^*$	$\beta^*$	$m$	$K_0$	$\tilde{\gamma}$	$\sigma_0/\text{MPa}$
87,273.57	1.90E7	252.4	1.47E-5	6.34	7.7634	0.4479	670.71

where,  $N$  is the number of stress-plastic strain data from the CAPSC test. The gradient descent algorithm continually updates the material parameters, as shown in Fig. 12. When the average error in the model prediction of stress is equal to or less than the limit value  $\delta$ , it demonstrates that the material parameters of the optimal solution are achieved so that the material parameters of the last  $i + 1$  step are output as the optimal solution. The results of the eight material parameters fitted by the algorithm are shown in Table 3. The fitting results are shown in Fig. 13 with a correlation coefficient ( $R^2$ ) of 0.96, demonstrating that the dislocation density evolution model frame can characterize the deformation hardening mechanism of 30CrMnSiA under non-current conditions.

### Dislocation density evolution constitutive model under different pulsed current conditions

The model is modified to incorporate the electroplastic effect in this section. Four parameters, namely,  $K_0$ ,  $\tilde{\gamma}$ ,  $m$ , and  $\sigma_0$ , highlighted in the blue box in Fig. 12,

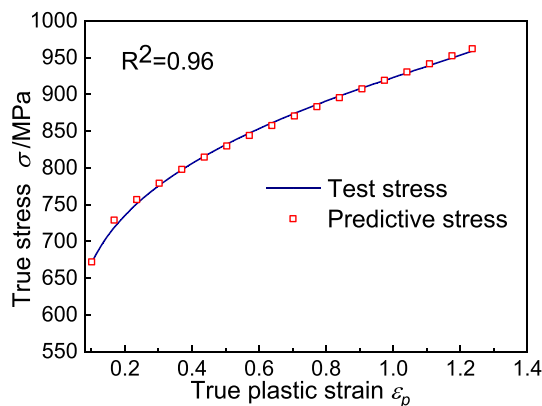


**Figure 13** Comparison between the test data and calculated true stress from the dislocation density evolution model under non-current condition.

are assigned as the material parameters related to the electroplastic effect. The material parameters listed in the orange box are considered material constants unrelated to the electroplastic effect.  $K_0$  represents the effect of the pulsed current on the dislocation annihilation rate, and  $\tilde{\gamma}$  represents the effect of the pulsed current on the grain refinement process. The influence of pulsed current on dislocation annihilation and grain size has been verified in Sect. 3.1.2 and several other literature sources [5, 13]. Furthermore, the parameter  $m$  can be affected by high-energy fields; thus, evaluating the influence of pulsed current on  $m$  is essential [45]. Studies have demonstrated that the electroplastic effect can modify the yield strength  $\sigma_0$  and is also characterized as a function of the pulsed current parameters [3].

The test data with pulsed current parameters of  $J_p = 1.25\text{--}5 \text{ A mm}^{-2}$  and  $d = 5\text{--}20\%$  served as the material parameter fitting group for the model. The test data with pulsed current parameters of  $J_p = 10\text{--}30 \text{ A mm}^{-2}$  and  $d = 20\%$  served as the validation group to evaluate the prediction accuracy of the constructed model. After fitting the stress–strain curves of the material parameter fitting group by the algorithm shown in Fig. 12, the material parameters of  $K_0$ ,  $\tilde{\gamma}$ ,  $m$ , and  $\sigma_0$  that vary with current parameters can be determined. It is necessary to construct the evolution equations of  $K_0$ ,  $\tilde{\gamma}$ ,  $m$ , and  $\sigma_0$  to determine the relationship between material parameters and the pulsed current parameters. The electroplastic effect is nearly proportional to the equivalent current density in the metal [46]. According to the classical electroplastic theory, the electron wind force per unit length of dislocation  $F_{ew}$  is proportional to the equivalent current density  $J_{rms}$ , which is [12, 47]:

$$F_{ew} = e \cdot n_e \cdot J_{rms} \cdot \frac{R}{\rho} \tag{14}$$

where,  $e$  and  $n_e$  represent the electron charge and density, and  $J_{rms}$  represents the equivalent current

density.  $R/\rho$  represents the resistivity per unit length of dislocation. The equation shows that the electrical wind force associated with the electroplastic effect mechanism is proportional to the equivalent current density. However, the stress reduction calculated by Eq. (14) is significantly less than the test data in numerous published papers [36]. One possible explanation is that the  $e$ ,  $n_e$ , and  $R/\rho$  are difficult to determine precisely during the deformation. In addition, the electron wind force mechanism does not consider the local Joule heating effect and energy exchange between electrons and dislocations caused by electron motion [12]. Although the mechanism of the electroplastic effect is not completely understood, the electroplastic effect is always associated with  $J_{rms}$  [3, 13, 14]. Therefore, this study adopts the equivalent current density  $J_{rms}$  as a measure of the electroplastic effect, which is calculated as follows [48]:

$$J_{rms} = \lim_{T \rightarrow \infty} \sqrt{\frac{1}{2T} \int_{-T}^T [f(t)]^2 dt} = J_p \sqrt{d} \tag{15}$$

Figure 14 shows the relationship between  $J_{rms}$  and the parameters  $K_0$ ,  $\tilde{\gamma}$ ,  $m$ , and  $\sigma_0$ .  $K_0$  increases with the increase of  $J_{rms}$ .  $\sigma_0$  and  $\tilde{\gamma}$  decrease with the increase of  $J_{rms}$ . However, when  $J_{rms}$  approaches a high value, they all approach stability. As a result, an exponential function can fit the effect of current density on  $K_0$ ,  $\tilde{\gamma}$ , and  $\sigma_0$ . The product of the exponential function and the sine/cos function is employed to fit the  $m$  since the trend of  $m$  initially increases and subsequently decreases until it becomes stable. It is due to limited values for the effect of electroplasticity, as described in Sect. 3.1.2. The law of material parameters tends to be stable at the high current density region, which can also be observed in other research [3, 13]. Figure 14 also shows the best function fit results for the four parameters with red lines, and the empirical expressions of each fitting function are provided below:

$$K'_0 = \beta_1 + (\beta_2 - \beta_1) \cdot \exp\left(\frac{-J_{rms}}{\beta_3}\right) \tag{16}$$

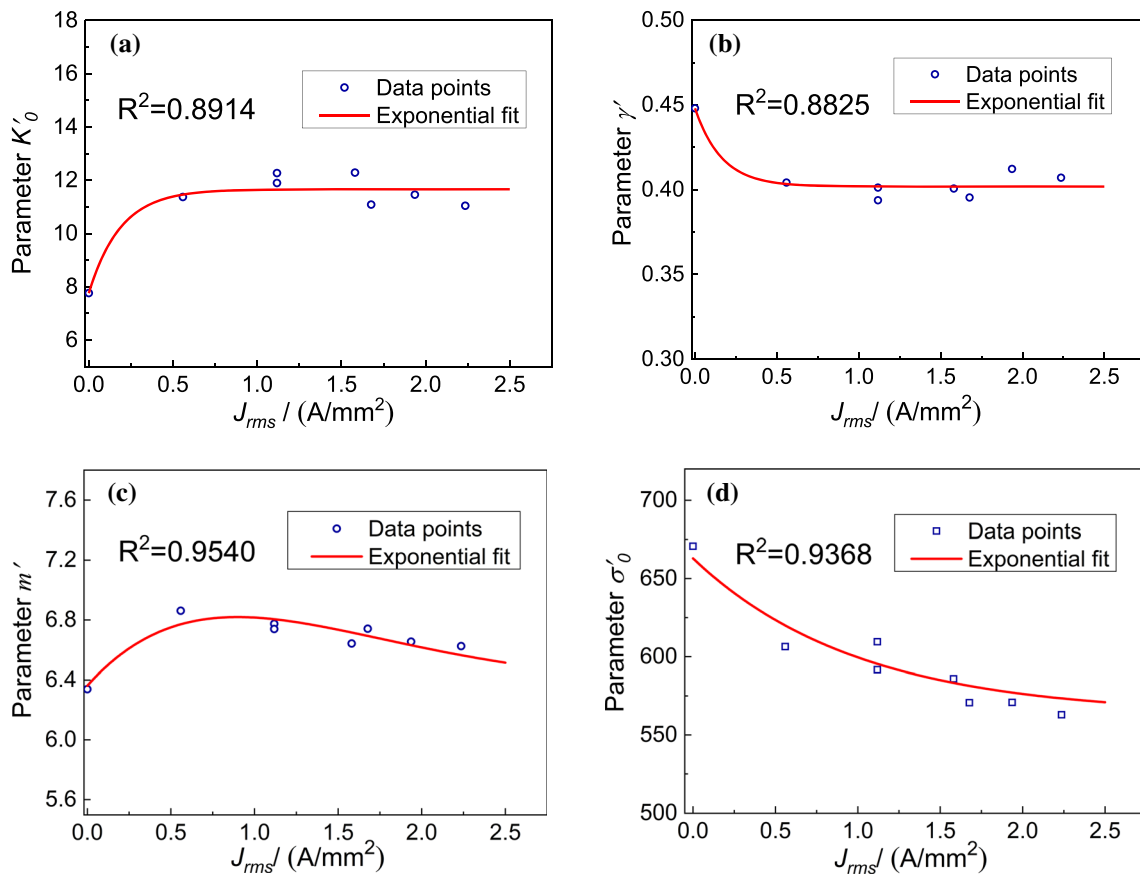


Figure 14 Best function fit of the model parameters: a  $K'_0$ , b  $\tilde{\gamma}$ , c  $m'$  and d  $\sigma_0$ .

$$\tilde{\gamma}' = \beta_4 + (\beta_5 - \beta_4) \cdot \exp\left(\frac{-J_{rms}}{\beta_6}\right) \tag{17}$$

$$m' = \exp(-a_1 \cdot J_{rms}) \cdot (a_2 \sin(a_1 \cdot J_{rms}) - a_3 \cos(a_1 \cdot J_{rms})) + a_4 \tag{18}$$

$$\sigma'_0 = \beta_7 + (\beta_8 - \beta_7) \cdot \exp(-J_{rms}) \tag{19}$$

where,  $K'_0$ ,  $\tilde{\gamma}$ ,  $m'$ , and  $\sigma'_0$  represent the material parameters considering the electroplastic effect, respectively.  $\beta_1 \sim \beta_8$  and  $a_1 \sim a_4$  are the fitting parameters of the constitutive model, as shown in Table 4.

### Accuracy evaluation of the model under different pulsed current conditions

Figure 15a and b shows the comparison of the model prediction with the test data under the different conditions of the fitting group. The result shows that the dislocation density evolution model considering the electroplastic effect presents a good agreement with test data under different pulsed current parameters, which indicates that the modified model can characterize the hardening behavior of 30CrMnSiA in the whole plastic deformation region with and without pulsed current. In addition, the predictive error of the model for the validation data group with the current parameters of  $J_p = 10\text{--}30 \text{ A mm}^{-2}$  and  $d = 20\%$  is also small, as shown in Fig. 15c. The correlation coefficient ( $R$ ) and the average relative error (AARE) are employed to evaluate the accuracy of the established constitutive model quantitatively [49]:

$$R = \frac{\sum_{i=1}^N (E_i - \bar{E}) \cdot (P_i - \bar{P})}{\sqrt{\sum_{i=1}^N (E_i - \bar{E})^2 \cdot \sum_{i=1}^N (P_i - \bar{P})^2}} \tag{20}$$

$$\text{AARE} = \frac{1}{N} \sum_{i=1}^N \left| \frac{E_i - P_i}{E_i} \right| \times 100\% \tag{21}$$

where,  $P_i$  and  $E_i$  represent the predictive stress of the constitutive model and test stress, respectively.  $\bar{P}$  and  $\bar{E}$  represent the average of predictive and test stress, respectively.  $N$  denotes the number of all stress-strain data. Figure 16 shows the correlation between

the predicted data and the test data. There are only slight differences between the test data and the predictions. The  $R$  and AARE for the fitting group are 0.994 and 0.811%, respectively. In addition, the  $R$  and AARE for the validation group are 0.974 and 4.56%, which implies that the constitutive model can accurately predict the plastic deformation behavior of 30CrMnSiA that takes the electroplastic effect into account. For simulation and process optimization of the CAFS, the dislocation density evolution constitutive model has excellent high accuracy over a wide plastic strain range under the electroplastic effect.

### Conclusion

The pulsed current-assisted deformation behavior of 30CrMnSiA was investigated by the CAPSC test, and the microstructure difference of the deformed specimens under non-current and pulsed current conditions was analyzed based on EBSD technology, a dislocation density evolution model considering microstructure evolution and the electroplastic effect was proposed to describe the hardening behavior under different pulsed current parameters. The main conclusions are as follows:

1. The effect of pulsed current on stress reduction positively correlates with increasing pulsed current parameters but decreases until it becomes stable beyond certain current parameter values. With  $J_p = 0\text{--}5 \text{ A mm}^{-2}$  and  $d = 0\text{--}15\%$ , the true stress gradually declines as  $J_p$  and  $d$  increase. However, the stress reduction rate slows significantly when  $J_p$  increases from 5 to 30  $\text{A mm}^{-2}$  at  $d$  equal to 20%, or when  $d$  increases from 15 to 20% at  $J_p$  equal to 5  $\text{A mm}^{-2}$ . This indicates that the electroplastic effect of 30CrMnSiA has a saturation limit under the condition of insignificant thermal effect.
2. Under plane strain deformation, the recovery mechanism induced by the pulsed current promotes the transition of the dislocation cell inside the grains to HAGBs, resulting in the reduction of GND and the enhancement of the proportion of fine grains under PC conditions. The proportion

**Table 4** Coefficients of parameter evolution functions

$\beta_1$	$\beta_2$	$\beta_3$	$\beta_4$	$\beta_5$	$\beta_6$	$\beta_7$	$\beta_8$	$a_1$	$a_2$	$a_3$	$a_4$
11.66	7.761	0.1882	0.4018	0.448	0.1634	562.7	662.9	0.9169	1.312	0.05043	6.412

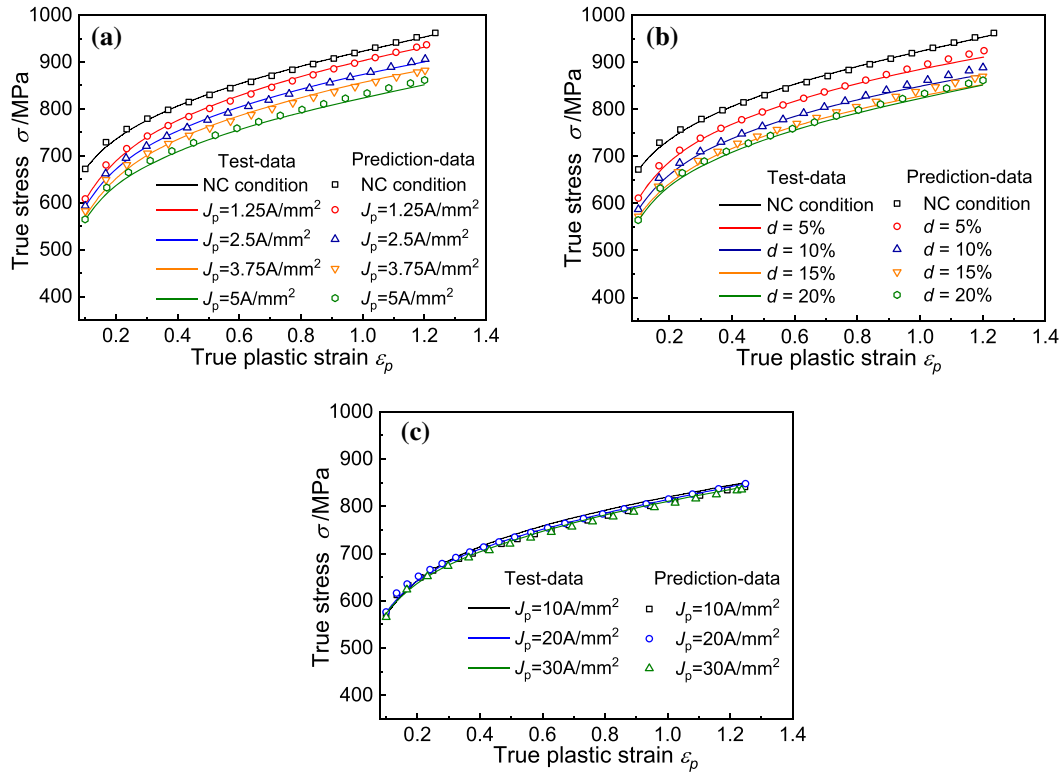


**Figure 15** Comparison between the Predicted stress and measured stress under different current parameters: **a**  $J_p = 1.25\text{--}5\text{ A mm}^{-2}$  with  $d = 20\%$ , **b**  $J_p = 5\text{ A mm}^{-2}$  with  $d = 5\text{--}20\%$ , and **c**  $J_p = 10\text{--}30\text{ A mm}^{-2}$  with  $d = 20\%$ .

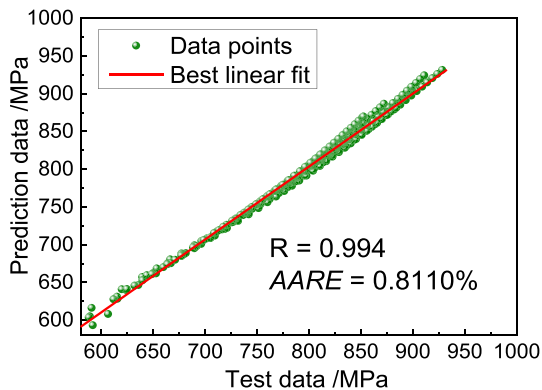


**Figure 16** Correlation between the test and calculated true stress.

of both LAGBs and HAGBs was significantly higher in the PC condition compared to the NC condition at  $\varepsilon_p = 1.2$ , indicating that the pulsed current leads to more effective grain refinement. The PC condition also yielded 45.5% fine grains after deformation, up from 31.7% in the NC condition.

3. A modified dislocation density evolution model that accurately captures the flow behavior of 30CrMnSiA during CAPSC by incorporating the

coupling effect of the grain refinement mechanism and the electroplastic effect. The model employs independent evolution functions to describe the evolution of dislocation density in the interior and at the grain boundary during the LAGBs to HAGBs transformation. The correlation coefficient and the average relative error for the validation group are 0.974 and 4.56%, respectively, which indicates that the modified constitutive model can accurately predict the plastic deformation behavior during the CAF process.

## Acknowledgements

This work was financially supported by the National Natural Science Foundation of China (52175316); the Natural Science Foundation of Basic and Applied Basic Research of Guangdong Province (2021A1515011074); Guangdong Science and Technology Special Fund Project (210907154533470) and the Guangdong Province Key Laboratory of Precision Equipment and Manufacturing Technology (PEMT1202).



## Author contributions

QXX: Supervision, Conceptualization, Methodology, Validation, Investigation, Resources, Data Curation, Writing—Review and Editing, Visualization, Project administration, Funding acquisition. CC: Conceptualization, Methodology, Software, Validation, Formal analysis, Investigation, Data Curation, Writing—Original Draft, Visualization. GFX: Conceptualization, Methodology, Validation, Investigation, Writing—Review and Editing. KWC: Validation, Data Curation. HYZ: Validation, Data Curation.

## Declarations

**Conflict of interest** The Authors have no conflict of interest to disclose.

## References

- [1] Liu T, Shi X, Zhang J, Fei B (2019) *Int J Fatigue* 122:240–255. <https://doi.org/10.1016/j.ijfatigue.2019.02.001>
- [2] Hariharan K, Lee M-G, Kim M-J, Han HN, Kim D, Choi S (2015) *Metall and Mater Trans A* 46:3043–3051. <https://doi.org/10.1007/s11661-015-2879-3>
- [3] Zhao YC, Wan M, Meng B, Xu J, Shan DB (2019) *Mater Sci and Eng: A* 767:138412. <https://doi.org/10.1016/j.msea.2019.138412>
- [4] Zhan L, Ma Z, Zhang J, Tan J, Yang Z, Li H (2016) *J Alloys Compd* 679:316–323. <https://doi.org/10.1016/j.jallcom.2016.04.051>
- [5] Zhang X, Li H, Zhan M (2018) *J Alloys Compd* 742:480–489. <https://doi.org/10.1016/j.jallcom.2018.01.325>
- [6] Zhao J, Wang GX, Dong Y, Ye C (2017) *J Appl Phys* 122:085101. <https://doi.org/10.1063/1.4998938>
- [7] Zhao S, Zhang R, Chong Y et al (2021) *Nat Mater* 20:468–472. <https://doi.org/10.1038/s41563-020-00817-z>
- [8] Xiao G, Xia Q, Cheng X, Long H (2016) *Sci China Technol Sci* 59:1656–1665. <https://doi.org/10.1007/s11431-016-0206-6>
- [9] Souza PM, Sivaswamy G, Bradley L, Barrow A, Rahimi S (2022) *J Mater Sci* 57:20794–20814. <https://doi.org/10.1007/s10853-022-07906-1>
- [10] Meng T, Dong C, Peng C, Wang R, Feng Y (2022) *J Mater Sci* 57:717–730. <https://doi.org/10.1007/s10853-021-06601-x>
- [11] Chen Z-J, Lin YC, He D-G, Lou Y-M, Chen M-S (2021) *Mater Sci Eng A* 827:142062. <https://doi.org/10.1016/j.msea.2021.142062>
- [12] Krishnaswamy H, Kim MJ, Hong S-T et al (2017) *Mater Des* 124:131–142. <https://doi.org/10.1016/j.matdes.2017.03.072>
- [13] Liu YZ, Wan M, Meng B (2021) *Int J Mach Tools Manuf* 162:103689. <https://doi.org/10.1016/j.ijmachtools.2021.103689>
- [14] Xu Z, Jiang T, Huang J, Peng L, Lai X, Fu MW (2022) *Int J Mach Tools Manuf* 175:103871. <https://doi.org/10.1016/j.ijmachtools.2022.103871>
- [15] Kim M-J, Yoon S, Park S et al (2020) *Appl Mater Today* 21:100874. <https://doi.org/10.1016/j.apmt.2020.100874>
- [16] Jiang T, Peng L, Yi P, Lai X (2017) *J Manuf Sci Eng* 139:011004. <https://doi.org/10.1115/1.4033904>
- [17] Chermette C, Unruh K, Peshekhodov I, Chottin J, Balan T (2019) *Int J Mater Form* 13:269–292. <https://doi.org/10.1007/s12289-019-01485-4>
- [18] Can C, Lei W, Xiao X, Qinxiang X (2020) *J Phys Conf Ser* 1605:012125. <https://doi.org/10.1088/1742-6596/1605/1/012125>
- [19] Liu X, Fan J, Li K et al (2021) *J Alloys Compd* 881:160648. <https://doi.org/10.1016/j.jallcom.2021.160648>
- [20] Xiao G, Zhu N, Long J, Xia Q, Chen W (2018) *J Manuf Processes* 34:140–147. <https://doi.org/10.1016/j.jmapro.2018.05.034>
- [21] Yin B, Xue X, Tang B, Wang Y, Kou H, Li J (2020) *Prog Nat Sci: Mater Int* 30:526–532. <https://doi.org/10.1016/j.pnsc.2020.08.007>
- [22] Annasamy M, Haghdadi N, Taylor A, Hodgson P, Fabijanic D (2019) *Mater Sci Eng, A* 745:90–106. <https://doi.org/10.1016/j.msea.2018.12.102>
- [23] A Standard (2010) ASTM international: West Conshohocken, PA, USA. <https://doi.org/10.1520/E0112-10>
- [24] Xia QX, Chen C, Xiao GF, Zhou HY (2022) *IOP Conf Ser Mater Sci Eng* 1270:012003. <https://doi.org/10.1088/1757-899X/1270/1/012003>
- [25] Ruskiewicz BJ, Grimm T, Ragai I, Mears L, Roth JT (2017) *J Manuf Sci Eng* 139:110801. <https://doi.org/10.1115/1.4036716>
- [26] Hielscher R, Silbermann CB, Schmidl E, Ihlemann J (2019) *J Appl Crystallogr* 52:984–996. <https://doi.org/10.1107/s1600576719009075>
- [27] Jiang Y-Q, Lin YC, Wang G-Q, Pang G-D, Chen M-S, Huang Z-C (2021) *J Alloys Compd* 870:159534. <https://doi.org/10.1016/j.jallcom.2021.159534>
- [28] Magargee J, Fan R, Cao J (2013) *J Manuf Sci Eng* 135:061022. <https://doi.org/10.1115/1.4025882>
- [29] Kumar W, Sharma UK, Shome M (2021) *J Constr Steel Res* 181:106615. <https://doi.org/10.1016/j.jcsr.2021.106615>
- [30] Liu K, Dong X, Xie H, Peng F (2015) *Mater Sci Eng A* 623:97–103. <https://doi.org/10.1016/j.msea.2014.11.039>

- [31] Molotskii M, Fleurov V (2000) *J Phys Chem B* 104:3812–3816. <https://doi.org/10.1021/jp993259g>
- [32] Gao J, Li H, Sun X, Zhang X, Zhan M (2022) *Int J Plast* 157:103397. <https://doi.org/10.1016/j.ijplas.2022.103397>
- [33] Wang X, Xu J, Shan D, Guo B, Cao J (2016) *Int J Plast* 85:230–257. <https://doi.org/10.1016/j.ijplas.2016.07.008>
- [34] Zhao W, Liu H, Outeiro J, Xu X, Zhang J (2020) *J Manuf Sci Eng* 142:091006. <https://doi.org/10.1115/1.4047431>
- [35] Borgh I, Hedström P, Persson T et al (2014) *Int J Refract Met Hard Mater* 43:205–211. <https://doi.org/10.1016/j.ijrmhm.2013.12.007>
- [36] Xiang S, Zhang X (2019) *Mater Sci Eng A* 761:138026. <https://doi.org/10.1016/j.msea.2019.138026>
- [37] Zheng F, Chen H, Wang W, Liu R, Lian J (2022) *J Mater Eng Perform* 31:6473–6486. <https://doi.org/10.1007/s11665-022-06705-8>
- [38] Qian L, Zhan L, Zhou B, Zhang X, Liu S, Lv Z (2021) *Mater Sci Eng A* 812:141144. <https://doi.org/10.1016/j.msea.2021.141144>
- [39] Waryoba D, Islam Z, Wang B, Haque A (2020) *J Alloys Compd* 820:153409. <https://doi.org/10.1016/j.jallcom.2019.153409>
- [40] Dong X, Shin YC (2019) *Int J Mech Sci* 150:576–583. <https://doi.org/10.1016/j.ijmecsci.2018.10.061>
- [41] Estrin Y, Toth LS, Molinari A, Bréchet Y (1998) *Acta Mater* 46:5509–5522
- [42] Ding H, Shen N, Shin YC (2012) *J Mater Process Technol* 212:1003–1013. <https://doi.org/10.1016/j.jmatprotec.2011.12.005>
- [43] Estrin Y, Kim HS (2007) *J Mater Sci* 42:1512–1516. <https://doi.org/10.1007/s10853-006-1282-2>
- [44] Lin YC, Wen D-X, Huang Y-C, Chen X-M, Chen X-W (2015) *J Mater Res* 30:3784–3794. <https://doi.org/10.1557/jmr.2015.368>
- [45] Ding H, Shen N, Shin YC (2011) *Comput Mater Sci* 50:3016–3025. <https://doi.org/10.1016/j.commatsci.2011.05.020>
- [46] Nguyen TT, Nguyen TV, Hong S-T, Kim M-J, Han HN, Morestin F (2016) *Adv Mater Sci Eng* 2016:1–10. <https://doi.org/10.1155/2016/9560413>
- [47] Tiwari J, Balaji V, Krishnaswamy H, Amirthalingam M (2022) *Int J Mech Sci* 227:107433. <https://doi.org/10.1016/j.ijmecsci.2022.107433>
- [48] Zhao J, Ren Z, Zhang H, Wang G-X, Dong Y, Ye C (2019) *J Appl Phys* 125:185104. <https://doi.org/10.1063/1.5087465>
- [49] Lin YC, Wen D-X, Chen M-S, Chen X-M (2016) *J Appl Phys* 122:805. <https://doi.org/10.1007/s00339-016-0333-z>

**Publisher's Note** Springer Nature remains neutral with regard to jurisdictional claims in published maps and institutional affiliations.

Springer Nature or its licensor (e.g. a society or other partner) holds exclusive rights to this article under a publishing agreement with the author(s) or other rightsholder(s); author self-archiving of the accepted manuscript version of this article is solely governed by the terms of such publishing agreement and applicable law.